Journal of Materials Chemistry A

ROYAL SOCIETY OF CHEMISTRY

COMMUNICATION

View Article Online
View Journal | View Issue

Cite this: J. Mater. Chem. A, 2023, 11, 9762

Received 19th February 2023
Accepted 12th April 2023

DOI: 10.1039/d3ta01029e

rsc.li/materials-a

Understanding and unlocking the role of V in boosting the reversible hydrogen storage performance of MgH_2†

Yang Meng,[a] Jian Zhang,[b] Shunlong Ju,[a] Yaxiong Yang,[c] Zhenglong Li,[c] Fang Fang,[a] Dalin Sun,[a] Guanglin Xia, *[a] Hongge Pan [c] and Xuebin Yu*[a]

Although MgH_2 is widely regarded as one of the most promising solid-state hydrogen storage materials, the high operating temperature and sluggish kinetics of hydrogenation and dehydrogenation are major challenges for its practical application. Herein, V_6O_{13} nanobelts with a thickness of 11 nm are fabricated to promote the reversible hydrogen storage performance of MgH_2. The favorable interaction between V_6O_{13} nanobelts and MgH_2 leads to *in situ* homogeneous formation of metallic V during the initial dehydrogenation of MgH_2. Induced by the catalysis of metallic V, which results in weaker structural stability and higher surface states of MgH_2 attributed to the strong bonding interactions between V and H, the energy required for H_2 desorption from MgH_2 is decreased to 49.5 kJ mol^{-1}, 10.9 kJ mol^{-1} lower than that of pristine MgH_2. Moreover, during the reversible hydrogenation process, the catalysis of metallic V lowers the energy for H_2 adsorption and dissociation on Mg down to −5.904 and 0.023 eV, respectively, while those values reach −0.086 and 1.103 eV for pristine Mg. As a result, with the introduction of V_6O_{13} nanobelts with an ultralow content of 3 wt%, a systematic hydrogen storage capacity of 6.8 wt% could be retained at 250 °C after 10 cycles.

1. Introduction

As a sustainable and clean energy source, hydrogen energy is undoubtedly one of the best choices for future low-carbon energy systems.[1] Efficient and safe storage of hydrogen with high gravimetric and volumetric capacity poses a major bottleneck for the development of hydrogen energy.[2–5] Due to its high theoretical volumetric and gravimetric storage density (110 g L^{-1} and 7.6 wt%) and low price, magnesium hydride (MgH_2) is considered as one of the most ideal solid hydrogen storage materials.[6–8] Unfortunately, induced by the high thermodynamic stability and kinetic barrier, the operating temperature for the reversible hydrogen storage of MgH_2 is in general over 400 °C, which hinders its commercial applications for on-board hydrogen storage.[9,10]

To date, the introduction of transition metal based catalysts that have a unique 3d electronic structure, especially V-based compounds, is regarded as one of the most effective strategies to enhance the hydrogen storage performance of MgH_2.[10–18] It has been widely verified that transition metal-based catalysts could alleviate the dissociation energy of hydrogen on the surface of Mg, which would significantly improve the hydrogen adsorption kinetics of Mg.[19–25] The interaction between the unsaturated d electrons of transition metals and the H 1s electron, on the other hand, could weaken the Mg–H bonds of MgH_2, which would enhance the hydrogen desorption performance of MgH_2.[26–30] As a result, various strategies have been proposed to further realize and improve the catalytic effect of V-based catalysts, *e.g.*, the building of nanostructured catalysts,[31–33] the construction of bimetallic catalytic systems, *etc.*[18,34–37] During the reversible H_2 desorption and adsorption process of MgH_2, V-based compounds would be reduced to low-valence metal compounds or even zero-valence metals, which are regarded as real catalysts in the system,[38–41] accompanied by the irreversible formation of Mg-based byproducts (*e.g.*, MgO, $MgCl_2$, MgS, *etc.*) that are inactive for hydrogen storage. The consumption of MgH_2 during the reduction of V-based compounds would lead to continuous degradation of reversible hydrogen storage capacity and more importantly, the balance between the amount of catalysts and the hydrogen storage performance of MgH_2 is difficult to reach in general. Therefore, although it has long been demonstrated that the catalytic effect of V in enhancing the hydrogen storage performance of MgH_2 is much better than that of other transition metals,[42,43] such as Nb, Zr, Ti, Sc and Y, the performance of

[a]Department of Materials Science, Fudan University, Shanghai 200433, China. E-mail: xiaguanglin@fudan.edu.cn; yuxuebin@fudan.edu.cn

[b]Hunan Provincial Key Laboratory of Intelligent Manufacturing Technology for High-performance Mechanical Equipment, Changsha University of Science and Technology, Changsha 410114, China

[c]Institute of Science and Technology for New Energy, Xi'an Technological University, Xi'an 710021, China

† Electronic supplementary information (ESI) available. See DOI: https://doi.org/10.1039/d3ta01029e

MgH_2 catalyzed by V-based compounds is far behind that achieved recently by the catalysis of other transition metal-based compounds.

Herein, to unleash the potential of V-based catalysts in improving the hydrogen storage performance of MgH_2, uniform two-dimensional V_6O_{13} nanobelts with a thickness of only 11 nm, which could facilitate the homogeneous distribution of V_6O_{13} nanobelts inside of the MgH_2 matrix to maximize their catalytic effect, are fabricated. It is theoretically and experimentally demonstrated that metallic V that would be *in situ* formed during the hydrogen desorption of MgH_2 could not only promote the H_2 desorption process from MgH_2, but also facilitate its H_2 adsorption process. Induced by the strong bonding interaction between V and H that is capable of effectively weakening the Mg–H bonds of MgH_2, the H_2 desorption energy for MgH_2 under the catalysis of metallic V is decreased to only 49.5 kJ mol^{-1}, 10.9 kJ mol^{-1} lower than that of pristine MgH_2. Moreover, during the reversible hydrogenation process, the energy required for H_2 adsorption and dissociation on Mg catalyzed by metallic V is significantly reduced to −5.904 and 0.0234 eV, respectively, while those values reach −0.086 and 1.103 eV for pristine Mg, indicating its remarkably catalytic effect for the H_2 adsorption of MgH_2 attributed to the weaker structural stability and higher surface states. As a result, with the addition of V_6O_{13} nanobelts with an ultralow content of 3 wt%, the peak temperature of H_2 desorption of MgH_2 decreases to 221 °C, 101 °C lower than that of pristine MgH_2 and, even at room temperature, approximately 5.4 wt% H_2 could be reversibly charged into the dehydrogenated MgH_2 within 12 h. More impressively, a systematic H_2 storage capacity of 6.8 wt% is preserved after 10 cycles at 250 °C.

2. Results and discussion

As schematically illustrated in Fig. 1a, V_6O_{13} nanobelts were synthesized by a facile two-step process including hydrothermal reaction and calcination under argon. The phase analysis of as-synthesized catalysts is first performed by X-ray diffraction (XRD). As shown in the XRD patterns, the characteristic diffraction peaks of the product after hydrothermal reaction and after calcination could be indexed to $NH_4V_4O_{10}$ and V_6O_{13} (Fig. S1† and 1b), respectively, which are the direct proofs of the successful synthesis of V_6O_{13}. The high-resolution V 2p X-ray photoelectron spectroscopy (XPS) patterns exhibit that the bimodal peaks at 516.2/523.1 eV and 517.3/524.5 eV (ref. 44 and 45) could be indexed to V^{4+} and V^{5+} (Fig. 1c), respectively, demonstrating the successful synthesis of V_6O_{13}. The morphologies of as-prepared catalysts are first investigated by scanning electron microscopy (SEM). SEM images validate that as-prepared $NH_4V_4O_{10}$ is composed of nanobelts (Fig. S2†) and its morphology is preserved perfectly after thermal treatment (Fig. 1d and S3†). Transmission electron microscopy (TEM) is used to further observe the morphology of the products. TEM images verify that the length, width, and thickness of V_6O_{13} nanobelts are limited to be only 500, 50, and 11 nm, respectively (Fig. 1e and S4†). The lattice fringes of 5.85 Å could be clearly observed from the high-resolution TEM (HRTEM) images, which could be indexed to the (200) plane of V_6O_{13} (inset of Fig. 1f and S5†), corresponding well to the relative XRD and XPS results. The formation of V_6O_{13} nanobelts, which could be additionally verified by the scanning TEM (STEM) image, would facilitate homogeneous distribution of V_6O_{13} inside of the system during the ball-milling process, therefore leading to promoted catalytic effect of V_6O_{13} in boosting the hydrogen storage properties of MgH_2. As illustrated in Fig. 1g, the homogeneous dispersion of V and O elements in V_6O_{13} nanobelts could be confirmed by the energy dispersive spectroscopy (EDS) elemental mapping images, while bulk V_6O_{13} is composed of irregular particles of tens of microns in size as evidenced by SEM images (Fig. S6†).

The catalytic effect of V_6O_{13} nanobelts in facilitating the hydrogen desorption process of MgH_2 is estimated using the mixture of V_6O_{13} nanobelts and MgH_2. After ball milling, as shown in XRD patterns, the dominant characteristic diffraction peaks belong to MgH_2, while weak peaks of MgO are also detected (Fig. S7†), demonstrating partial reaction between MgH_2 and V_6O_{13} nanobelts during the process of ball milling. Unfortunately, owing to the low content and *in situ* reaction, the diffraction peaks of V_6O_{13} nanobelts could not be observed. After the ball milling process, SEM and TEM images exhibit that the mixture of MgH_2 and V_6O_{13} nanobelts is irregular, 100 to 500 nm particles in size, which is basically consistent with that of pristine MgH_2 (Fig. S8 and S9†). EDS elemental mapping analysis (Fig. S10†) verifies the uniform dispersion of V, Mg, and O in the ball-milled composites, directly demonstrating the uniform distribution of V_6O_{13} in the system.

The dehydrogenation properties of MgH_2 catalyzed by V_6O_{13} nanobelts are evaluated by temperature programmed desorption (TPD) measurements. The initial and terminal temperatures of ball-milled MgH_2 are about 285 and 360 °C (Fig. 2a), respectively, and the H_2 capacity could finally approach 7.5 wt%, corresponding well to the theoretical H_2 capacity of MgH_2. For MgH_2 mixed with 10 wt% bulk V_6O_{13}, the initial and peak dehydrogenation temperatures could be reduced to 204 and 237 °C, respectively, indicating the impressive catalytic effect of V_6O_{13} in facilitating the H_2 desorption process of MgH_2. In strong contrast, upon decreasing the weight percent of V_6O_{13} nanobelts to only 5 wt%, the initial dehydrogenation temperature of MgH_2 could significantly lower to 208 °C (Fig. S11†), indicating that the building of nanobelts that could induce the uniform distribution of V_6O_{13} nanobelts in the system effectively improves the catalytic effect of V_6O_{13} towards enhancing the H_2 desorption performance. The initial and peak temperatures for H_2 to desorb from MgH_2 mixed with 15 wt% V_6O_{13} nanobelts are comparable with those of MgH_2 mixed with 10 wt% V_6O_{13} nanobelts (Fig. S11†), while MgH_2 catalyzed by 15 wt% V_6O_{13} nanobelts has a lower capacity of hydrogen storage. Hence, MgH_2 catalyzed by 10 wt% V_6O_{13} nanobelts is chosen for subsequent investigation in detail. Impressively, under the catalysis of 10 wt% V_6O_{13} nanobelts, MgH_2 starts liberating H_2 at only 180 °C, 24 °C lower than that of MgH_2 mixed with bulk V_6O_{13}, and a H_2 capacity of about 6.5 wt% could be achieved at 250 °C (Fig. 2a).

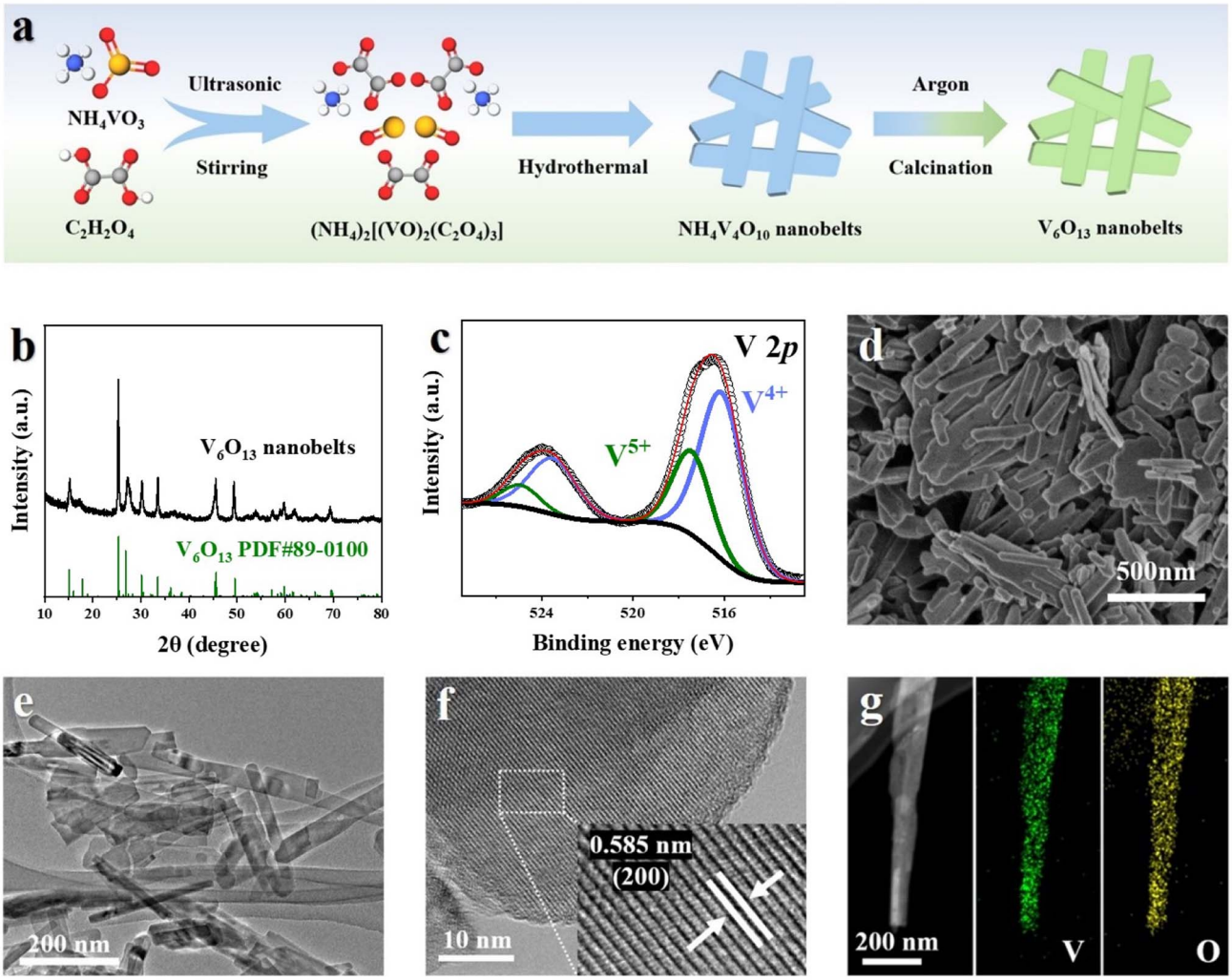

Fig. 1 (a) Schematic illustration of the synthesis process of as-synthesized V_6O_{13} nanobelts. (b) XRD pattern, (c) High-resolution V 2p XPS spectra, (d) SEM images, (e) TEM images, (f) HRTEM images, and (g) STEM and the relative EDS elemental mapping images of as-synthesized V_6O_{13} nanobelts.

Isothermal hydrogenation kinetics of MgH_2 catalyzed by V_6O_{13} nanobelts are subsequently investigated. Hydrogen release could be hardly detected from pristine MgH_2 at a temperature of 250 °C (Fig. 2b), while MgH_2 catalyzed by bulk V_6O_{13} could dehydrogenate completely within about 25 min, further demonstrating the catalytic role of V_6O_{13} in facilitating the dehydrogenation properties of MgH_2. By contrast, the time for MgH_2 catalyzed by V_6O_{13} nanobelts to dehydrogenate completely requires only 5 min, which further demonstrates the key role of the building structure of nanobelts in promoting the catalytic role of V_6O_{13}. When the thermal temperature was increased up to 275 °C, MgH_2 catalyzed by V_6O_{13} nanobelts could dehydrogenate completely within only 2 min with a H_2 capacity of 6.3 wt% (Fig. 2c). Moreover, when the temperature decreases to 225 and 200 °C, MgH_2 under the catalysis of V_6O_{13} nanobelts is capable of releasing 5.9 and 3.6 wt% H_2 in 30 min, respectively. According to Kissinger's method, the apparent activation energy (E_a) is computed to quantitatively study the catalytic role of V_6O_{13} nanobelts in promoting the dehydrogenation kinetics of MgH_2. According to eqn (1),[46] T_m is the temperature corresponding to the maximum dehydrogenation rate, β is the heating rate, R is the gas constant and E_a is the apparent activation energy and.

$$\frac{d\left(\ln\beta/T_m^2\right)}{d(1/T_m)} = \frac{-E_a}{R} \quad (1)$$

Herein, the TPD curves and relative differential results of MgH_2 catalyzed by V_6O_{13} nanobelts with various heating rates are selected to determine the T_m (Fig. S12–S15†). The E_a of MgH_2 under the catalysis of V_6O_{13} nanobelts is computed to be 82.3 ± 2.5 kJ mol^{-1} (Fig. S16†) after linear fitting, corresponding to 58% of that of pristine MgH_2 (*i.e.*, 141.2 kJ mol^{-1}), directly demonstrating that the introduction of V_6O_{13} nanobelts could significantly enhance the dehydrogenation kinetics of MgH_2.

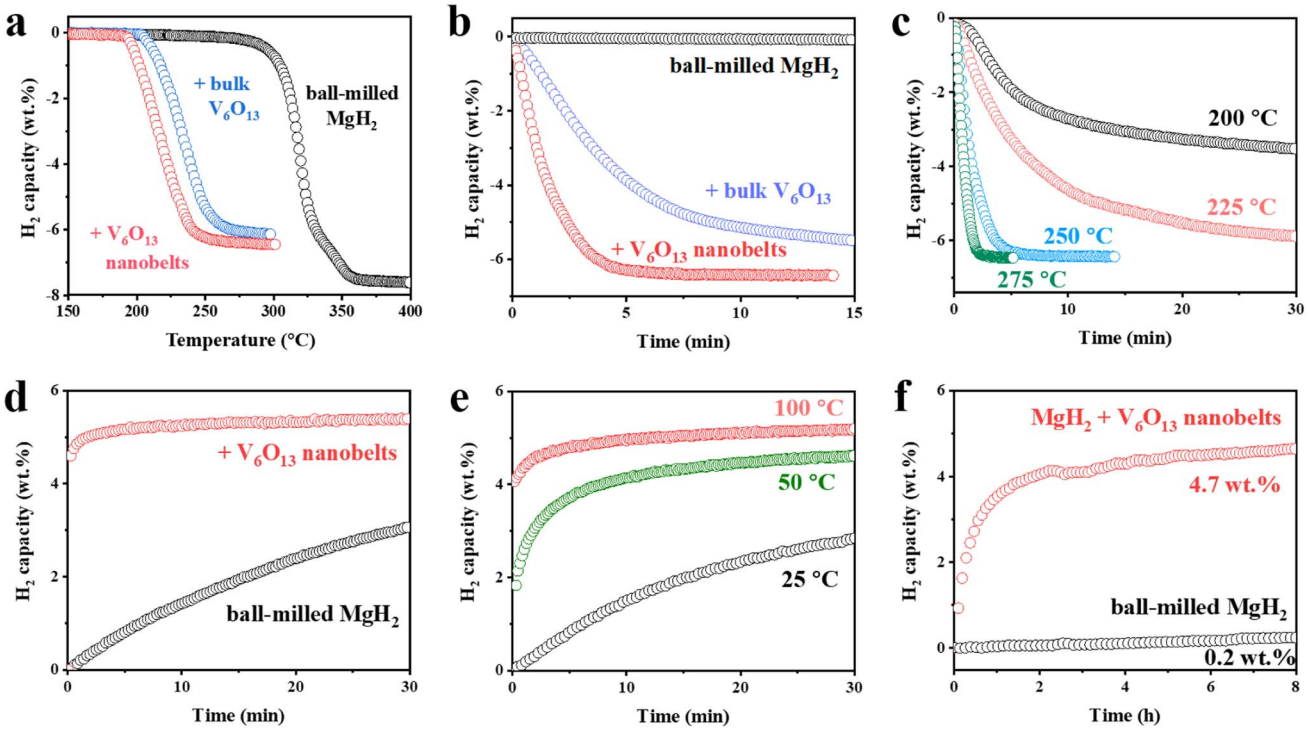

Fig. 2 (a) TPD results of MgH_2 under the catalysis of V_6O_{13} nanobelts, with ball-milled MgH_2 catalyzed by bulk V_6O_{13} included for comparison. (b) Isothermal H_2 desorption curves of MgH_2 catalyzed by V_6O_{13} nanobelts at 250 °C, with ball-milled MgH_2 under the catalysis of bulk V_6O_{13} included for comparison. (c) Isothermal H_2 desorption curves of MgH_2 catalyzed by V_6O_{13} nanobelts. (d) Isothermal H_2 adsorption curves of ball-milled MgH_2 and MgH_2 catalyzed by V_6O_{13} nanobelts at 150 °C. (e) Isothermal H_2 adsorption curves of MgH_2 under the catalysis of V_6O_{13} nanobelts. (f) Isothermal H_2 adsorption curves of MgH_2 without and with the addition of V_6O_{13} nanobelts at room temperature.

The reversible hydrogen adsorption measurement under a H_2 pressure of 50 atm at 50 °C illustrates that, after complete dehydrogenation, only 0.2 wt% H_2 could be adsorbed onto MgH_2 within 30 min, while 4.3 wt.% H_2 could be recharged into MgH_2 catalyzed by bulk V_6O_{13} within 30 min (Fig. S17†). This result indicates that V_6O_{13} could also enhance the H_2 adsorption properties of MgH_2. In strong contrast, after complete dehydrogenation, the H_2 readsorption capacity of MgH_2 could approach 4.7 wt%, which validates the excellent catalytic effect of V_6O_{13} nanobelts in promoting the hydrogenation process of MgH_2 compared to that of bulk V_6O_{13}. These results confirm that the uniform dispersion of V_6O_{13} nanobelts is capable of catalytically improving both hydrogenation and dehydrogenation properties of MgH_2. After complete dehydrogenation, at the temperature of 150 °C, approximately 5.1 wt% H_2 could be recharged into MgH_2 mixed with V_6O_{13} nanobelts in 100 s, while a small H_2 capacity of 0.5 wt% could be achieved for pristine MgH_2 at an identical temperature (Fig. 2d). It additionally confirms the catalytic effect of V_6O_{13} nanobelts in facilitating the hydrogenation process of MgH_2. After complete dehydrogenation, when the thermal temperature is down to 100 °C, about 5.2 wt% H_2 could be adsorbed onto MgH_2 catalyzed by V_6O_{13} nanobelts within 30 min (Fig. 2e). More impressively, even at room temperature, after complete dehydrogenation, approximately 4.7 wt% H_2 could be recovered to MgH_2 mixed with V_6O_{13} nanobelts in 8 h (Fig. 2f), corresponding to 81% of the initial H_2 capacity, while only approximately 0.2 wt% H_2 could be recharged into pure MgH_2 under identical conditions. This result provides additional evidence to the superior catalytic effect of V_6O_{13} nanobelts in enhancing the H_2 adsorption properties of MgH_2.

The dehydrogenation equilibrium pressure, which is validated by pressure–composition isotherm (PCI) curves (Fig. S18a†), could be intended to be about 0.3, 0.7, 1.2, and 2.5 atm at 250, 275, 300, and 325 °C, respectively. Under the catalysis of V_6O_{13} nanobelts, according to the van't Hoff equation,[47] the thermodynamic enthalpy (ΔH) of MgH_2 is computed to be 74.7 ± 2.8 kJ mol^{-1} (Fig. S18b†), corresponding well to that of ball-milled MgH_2, which indicates that V_6O_{13} nanobelts are ineffective in changing its thermodynamical stability. Hence, due to the impressive catalytic effect of V_6O_{13} nanobelts in improving its dehydrogenated and hydrogenated kinetics, the dehydrogenation and hydrogenation processes of MgH_2 have been greatly promoted.

After ten cycles of dehydrogenation and hydrogenation process, the reversible H_2 capacity of MgH_2 catalyzed by V_6O_{13} nanobelts could reach about 5.8 wt% (Fig. 3a), which could be confirmed by the cycling performance. The initial and terminal dehydrogenation temperatures of MgH_2 catalyzed by V_6O_{13} nanobelts after 10 cycles are basically consistent with those of the first cycle as verified by the relative TPD results (Fig. 3b). EDS elemental mapping images (Fig. S19†) reveal that the homogeneous dispersion of V inside of the MgH_2 matrix is maintained after 10 cycles, leading to stable dehydrogenation

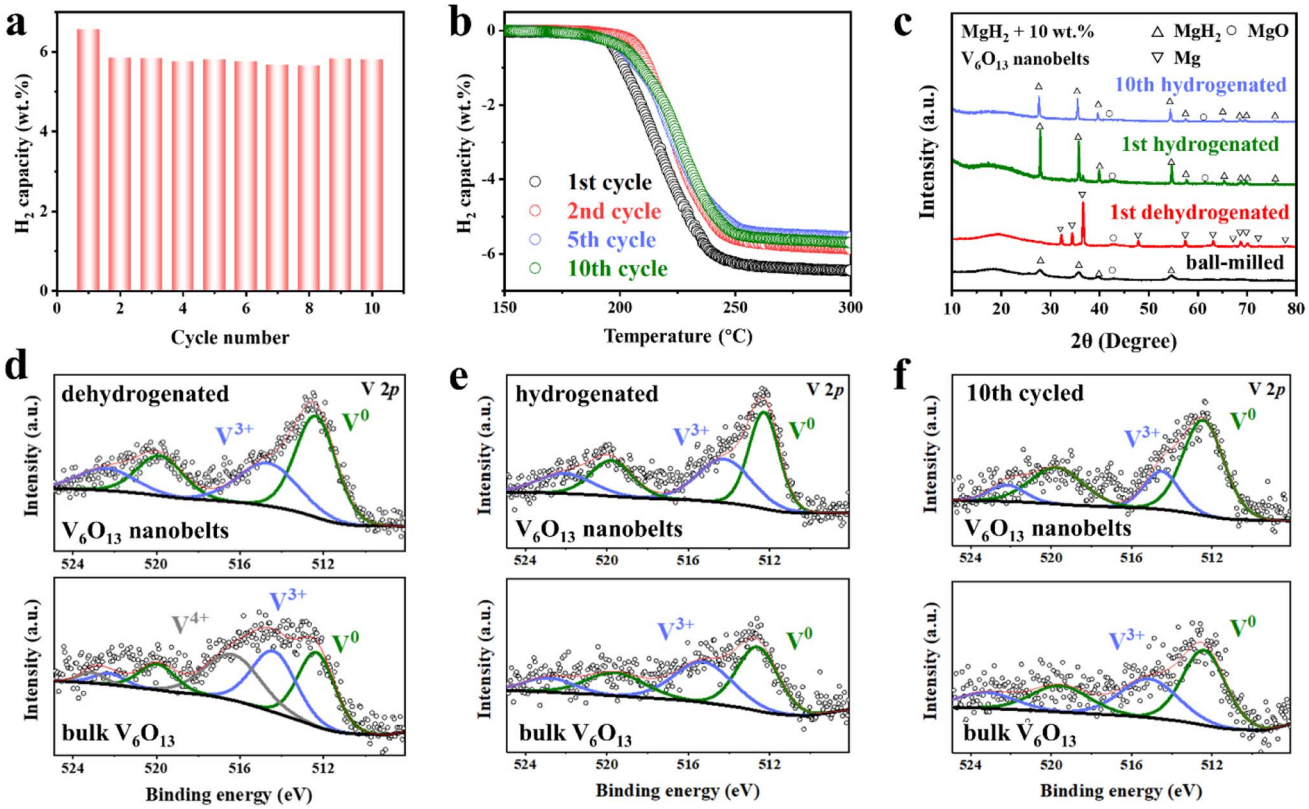

Fig. 3 (a) Reversible H_2 capacity and (b) the relative TPD results of MgH_2 under the catalysis of V_6O_{13} nanobelts upon cycling. (c) XRD patterns of MgH_2 under the catalysis of V_6O_{13} nanobelts at various states. (d–f) High-resolution V 2p XPS spectra of MgH_2 catalyzed by V_6O_{13} nanobelts and bulk V_6O_{13} at various states.

and hydrogenation performance of MgH_2. The chemical states of various samples are further investigated to understand the evolution of V_6O_{13} nanobelts during the reversible hydrogen storage process. XRD patterns reveal the reversible transformation between MgH_2 and Mg in the dehydrogenation and hydrogenation process (Fig. 3c). However, owing to the low content and/or *in situ* reduction of V_6O_{13} nanobelts, no diffraction peaks of V_6O_{13} nanobelts are observed from the XRD patterns. Fortunately, XPS analysis demonstrates that, during the ball milling process, partial high-valence V_6O_{13} is reduced with the formation of V^{3+} and metallic V (Fig. S20†).[32,36] After complete dehydrogenation in the first cycle, the valence state of V of V_6O_{13} nanobelts is further reduced with the disappearance of V^{5+} and V^{4+}, accompanied by the formation of metallic V and a small amount of V_2O_3 (Fig. 3d), indicating that V^{5+} and V^{4+} of V_6O_{13} nanobelts are *in situ* transformed to metallic V and V_2O_3. By comparison, partial high-valence V would be preserved after the dehydrogenation of MgH_2 catalyzed by bulk V_6O_{13}, indicating the weaker reduction capability of bulk V_6O_{13} than V_6O_{13} nanobelts inside of MgH_2. This result suggests that the smaller particle size also promotes the reduction of V_6O_{13} and hence the catalytic effect in facilitating the dehydrogenation and hydrogenation process of MgH_2. During the subsequent hydrogenation process, both V_6O_{13} nanobelts and bulk V_6O_{13} are *in situ* reduced to V_2O_3 and metallic V (Fig. 3e) and they are well preserved in the cycling process (Fig. 3f). Hence, metallic V and V_2O_3 could be regarded as the real catalyst for enhancing stable hydrogen storage performance of MgH_2. Furthermore, TPD measurements of commercial metallic V powder have been conducted (Fig. S21†), and under the catalysis of commercial metallic V powder, the onset temperature for the main dehydrogenation of MgH_2 is approximately 230 °C, 30 °C higher than that of MgH_2 catalyzed by V_6O_{13} nanobelts. This result indicates that the catalytic effect of *in situ* formed metallic V from the reaction between MgH_2 and V_6O_{13} nanobelts is better than that of bulk metallic V.

To understand structural evolution of MgH_2 catalyzed by V_6O_{13} nanobelts, TEM and HRTEM are subsequently conducted. As shown in Fig. 4, the visible lattice spacings of 0.245 and 0.251 nm are observed after dehydrogenation and hydrogenation in the initial cycle, which belong to the (101) planes of Mg and MgH_2, respectively, providing extra evidence to the reversible transformation of MgH_2 and Mg. After the initial dehydrogenation, new lattice spacings of 0.214 and 0.271 nm are verified and belong to the (110) plane of metallic V and the (104) plane of V_2O_3, respectively, which is consistent with the XPS results (Fig. 3d). Moreover, the characteristic lattice spacings of metallic V are uniformly distributed in the system, demonstrating the homogeneous dispersion of metallic V inside of MgH_2. After 10 cycles of H_2 desorption and adsorption process, the homogeneous distribution of metallic V and V_2O_3 is well

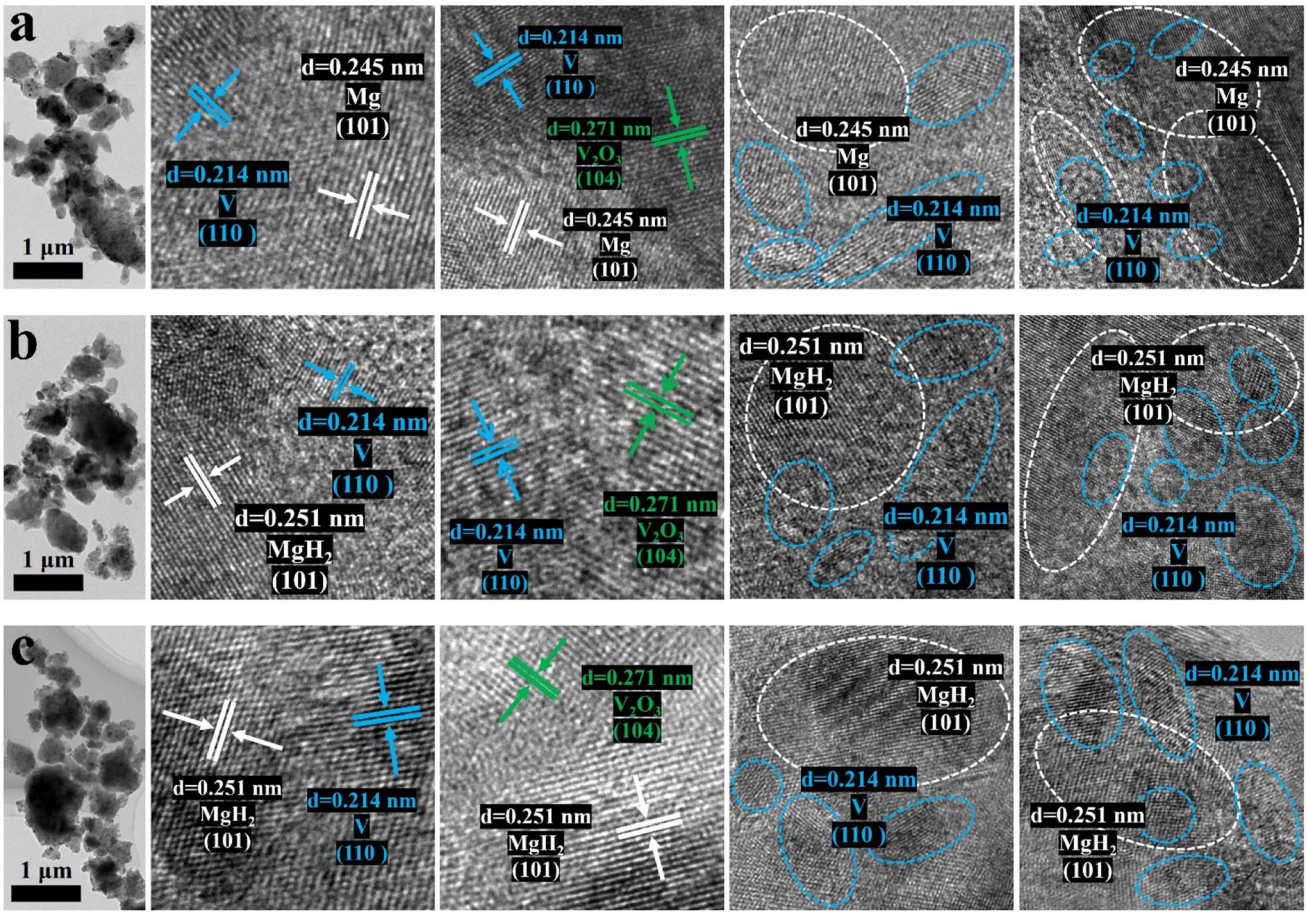

Fig. 4 TEM and the relative HRTEM images of MgH_2 under the catalysis of V_6O_{13} nanobelts after (a) dehydrogenation, (b) hydrogenation, and (c) 10 cycles of hydrogen storage process.

preserved, leading to stable reversibility of the dehydrogenation and hydrogenation process of MgH_2.

Based on density functional theory (DFT), theoretical calculations are conducted to unravel the catalytic role of metallic V and/or V_2O_3 in the hydrogen storage process of MgH_2. As shown in Fig. S22,† the length of Mg–H bonds in pure MgH_2 reaches 1.714 Å, and only limited changes of Mg–H bonds could be observed under the catalysis of V_2O_3, indicating the limited catalytic effect of V_2O_3 in enhancing the hydrogen storage performance of MgH_2. In strong contrast, under the catalysis of metallic V, the length of Mg–H bonds could be significantly extended to 3.116 and 2.046 Å, respectively, indicating the superior catalytic effect of metallic V to that of V_2O_3. Hence, the catalytic mechanism of V is further investigated in detail and the models of MgH_2 cells without and with the additional of V are provided in Fig. S23,† respectively. It is calculated that the desorption energy for H_2 from pristine MgH_2 reaches 60.4 kJ mol^{-1}, while the desorption energy drops down to approximately 49.5 kJ mol^{-1} for MgH_2 catalyzed by metallic V (Fig. 5a). These results indicate that the *in situ* formed metallic V during the cycling hydrogen storage process could effectively promote the dehydrogenation procedure of MgH_2, which could be verified by XPS and HRTEM results, corresponding well to the H_2 desorption results (Fig. 2a). The desorption of hydrogen from MgH_2 could be hypothesized as a two-step reaction (denoted as H^1 and H^2 atoms, respectively), and the calculated results are regarded as the removal energy of H atoms. The removal energy from pristine MgH_2 of both H^1 and H^2 atoms is computed to be 1.58 eV (Fig. 5b), indicating the high energy barrier for the dehydrogenation procedure of MgH_2, corresponding well to the high H_2 desorption temperature of pristine MgH_2. By comparison, for the H^1 and H^2 atoms of MgH_2 catalyzed by metallic V, the removal energies are decreased to 1.43 and 1.41 eV (Fig. 5b), respectively, which directly verifies its superior catalytic effect in improving the H_2 desorption performance. During the reversible H_2 adsorption process, the adsorption energy and dissociation energy barrier for H_2 on Mg (0001) is calculated to be about −0.086 and 1.103 eV (Fig. 5c and S24†), respectively, indicating the weak adsorption capacity and dissociation ability of H_2molecules on Mg, corresponding well to the slow H_2 adsorption rate and low hydrogen adsorption capacity of pure Mg. In strong contrast, the dissociation energy and adsorption energy barriers for H_2 on Mg (0001) with the addition of metallic V are only 0.023 and −5.904 eV (Fig. 5c and S24†), respectively, which are much lower than those of pristine

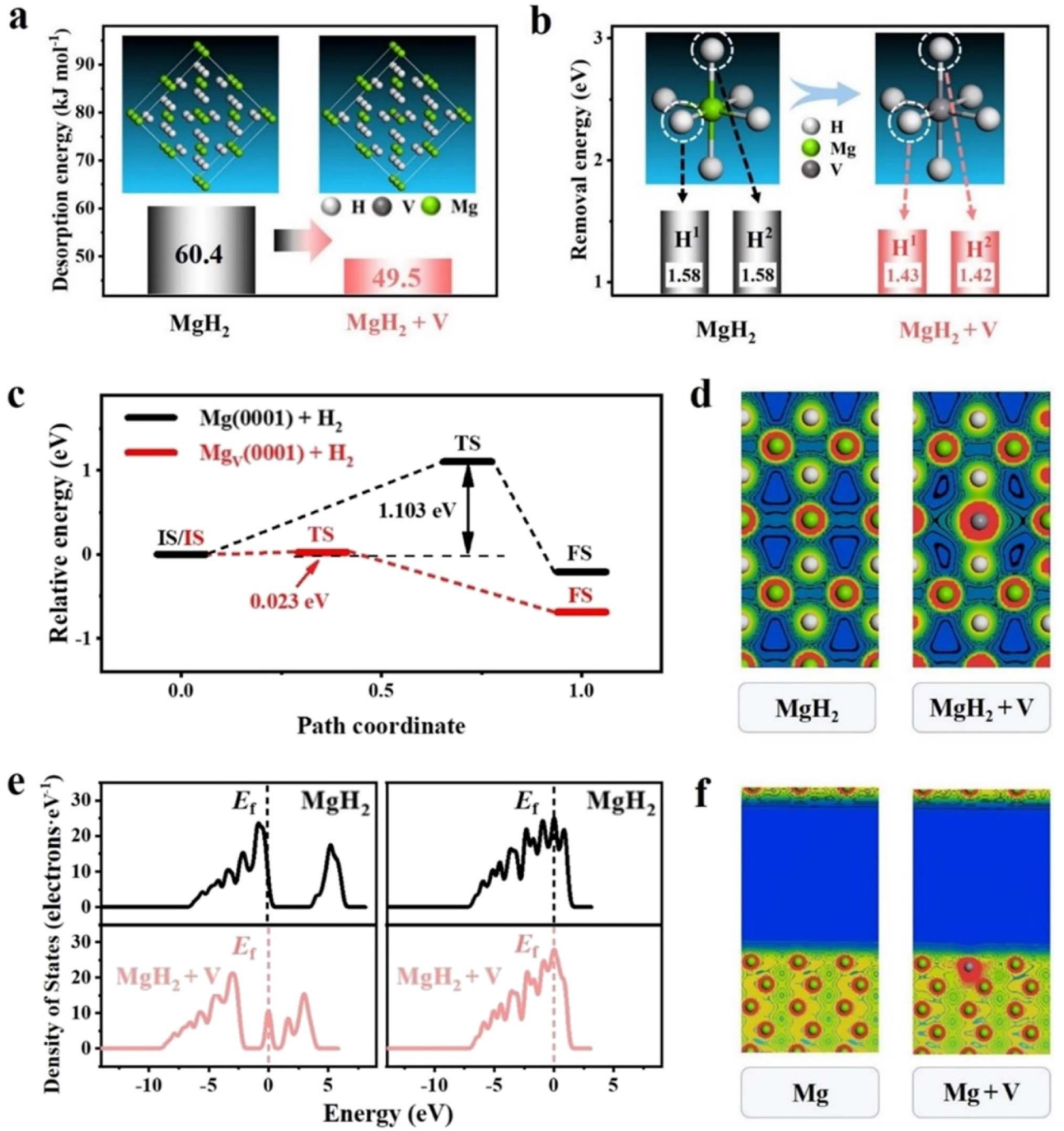

Fig. 5 (a) Calculated desorption energy profiles for the H_2 desorption of MgH_2 and MgH_2 doped with metallic V, respectively. (b) Calculated removal energy profiles for the removal of H^1 and H^2 from MgH_2 without and with the addition of metallic V, respectively. (c) Calculated dissociation energy barrier profiles for H_2 adsorption on Mg (0001), and Mg (0001) doped with metallic V, respectively. (d) Valence charge densities of pristine MgH_2 and MgH_2 doped with metallic V. (e) Total densities of states of Mg and MgH_2 doped with metallic V, with both pristine Mg and MgH_2 included for comparison. (f) Valence charge densities of pristine Mg and Mg doped with metallic V.

Mg, which is regarded as the direct verification of the catalytic role of V in promoting reversible hydrogenation of Mg.

Moreover, to reveal the mechanism of the sharp decline of the H_2 desorption and adsorption energy barrier induced by the catalysis of metallic V, the valence charge densities of Mg and MgH_2 with the addition of metallic V are investigated. Obvious charge transfer could be observed in pristine MgH_2 (Fig. 5d), leading to the presence of H negatively and Mg positively charged. In addition, the charge distribution around the H atom of MgH_2 is spherically symmetric, indicating the existence of strong ionic bonds between H and Mg, which should be responsible for the high removal energy of H atoms from MgH_2. Interestingly, after the addition of V atoms, the V atom shares charge with the adjacent H atoms and the charge distribution

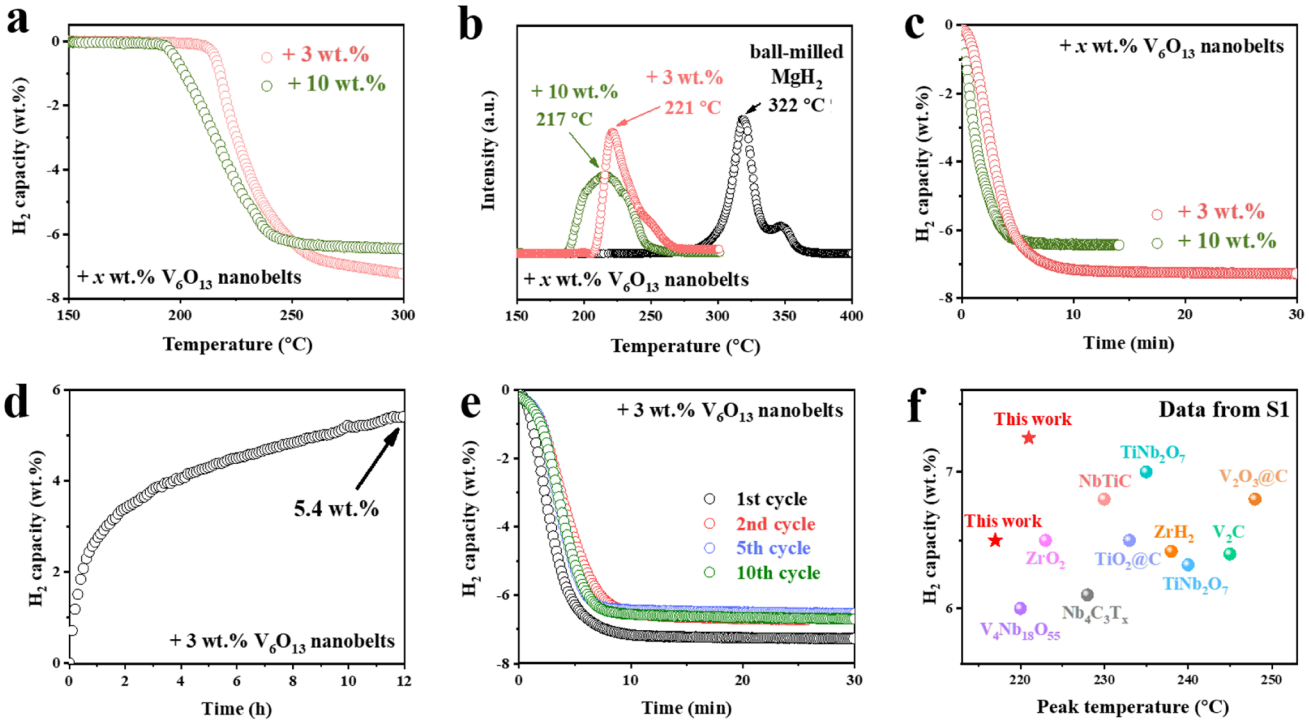

Fig. 6 (a) TPD results and (b) the relative derivative curves of MgH_2 with the weight percent of 3 and 10 wt% V_6O_{13} nanobelts. (c) Isothermal H_2 desorption curves of MgH_2 with the weight percent of 3 and 10 wt% V_6O_{13} nanobelts at 250 °C. (d) Isothermal H_2 adsorption curves of MgH_2 with the addition of 3 wt% V_6O_{13} nanobelts at room temperature. (e) Isothermal H_2 desorption curves of MgH_2 with the addition of 3 wt% V_6O_{13} nanobelts upon cycling at 250 °C. (f) The comparison of the amount of the catalysts, peak temperature, and H_2 desorption capacity of MgH_2 catalyzed by V_6O_{13} nanobelts with the state-of-the-art values reported recently using various catalysts.

around H atoms is directional, indicating the existence of covalent bonding interactions between V and H. These results demonstrate that the significant decrease of the removal energy of the H atom of MgH_2 induced by the doping of V could be attributed to the strong bonding between V atoms and adjacent H atoms, which weakens the Mg–H bond. The total densities of states (DOS), in which the Fermi level (E_f) is used as the reference and set as zero (Fig. 5e), illustrate that the total DOS of pristine MgH_2 is mainly distributed in the range of −6.6 to 6.7 eV, while it moves to a lower energy level after the introduction of V. More interestingly, the energy gap of MgH_2 with the introduction of the V atom near the E_f is narrower than that of pure MgH_2, which demonstrates that the doping of V leads to weaker structural stability of MgH_2 induced by the favorable bonding between the V atom and adjacent H atoms, resulting in lower energy required for hydrogen desorption from MgH_2.

In the case of pristine Mg, the electron cloud is relatively fat, while obvious sinking of the electrons on the top of the V atom could be observed for Mg after the doping of V (Fig. 5f), indicating that the doping of V is capable of enhancing the reactivity of Mg towards hydrogen adsorption. In addition, it could be observed that Mg (0001) doped with the V atom has higher surface states relative to Mg (0001) near the E_f in the total DOS plots (Fig. 5e) attributed to the contribution of the 3d orbitals of V atoms. It provides further evidence to the enhanced activity for H_2 dissociation on Mg induced by the doping of V, which accounts for the significant decline of the activation energy of H_2 dissociation on Mg. These results demonstrate the strong catalytic effect of V in enhancing the reversible dehydrogenation and hydrogenation performance of MgH_2, corresponding well to its lower operating temperature and rapid hydrogen storage kinetics. Hence, it could be demonstrated theoretically and experimentally that metallic V shows superior effective catalysis in the reversible hydrogenation and dehydrogenation process of MgH_2.

Unfortunately, it should be noted that, owing to the chemical reaction between V_6O_{13} nanobelts and MgH_2, the reversible H_2 storage capacity of MgH_2 mixed with 10 wt% V_6O_{13} nanobelts after 10 cycles is much lower than that of the first cycle (Fig. 3a and b). Reducing the amount of V_6O_{13} nanobelts should be an effective way to alleviate this negative effect and surprisingly, the catalytic effect of V_6O_{13} nanobelts is still capable of endowing MgH_2 with superior hydrogen storage performance when the weight percent of V_6O_{13} nanobelts is decreased down to only 3 wt%. As exhibited in Fig. 6a and b, mixed with 3 wt% V_6O_{13} nanobelts, the onset and peak dehydrogenation temperature of MgH_2 could lower to 210 and 221 °C. Although the onset dehydrogenated temperature of MgH_2 mixed with 3 wt% V_6O_{13} nanobelts is higher than that of MgH_2 mixed with 10 wt% V_6O_{13} nanobelts, the peak and terminal dehydrogenated temperatures of them are comparable. At the temperature of 250 °C, the isothermal H_2 desorption results illustrate that MgH_2 with the addition of 3 and 10 wt% V_6O_{13} nanobelts releases the same amount of H_2 within 5 min, while the capacity

of hydrogen released from MgH_2 under the catalysis of 3 wt% V_6O_{13} nanobelts reaches 7.25 wt% after prolonging the time to 10 min, 0.9 wt% higher than MgH_2 with the addition of 10 wt% V_6O_{13} nanobelts (Fig. 6c). Moreover, after complete dehydrogenation of MgH_2 under the catalysis of 3 wt% V_6O_{13}, even at room temperature, approximately 5.4 wt% H_2 could be reversibly adsorbed within 12 h (Fig. 6d), demonstrating that the reduction of the amount of V_6O_{13} nanobelts could still retain the superior low temperature H_2 adsorption performance. More importantly, the cycling performance verifies that, owing to the addition of V_6O_{13} nanobelts with an ultralow content of 3 wt%, the reversible H_2 capacity of this system could reach 6.8 wt% after ten cycles of hydrogen storage process at 250 °C (Fig. 6e), which is 1.0 wt% higher than that of MgH_2 catalyzed by 10 wt% V_6O_{13} nanobelts. These results directly demonstrate that, owing to the unique structure of V_6O_{13} nanobelts that ensures the uniform distribution of *in situ* formed metallic V inside of MgH_2, the catalytic effect of V_6O_{13} nanobelts could be effectively preserved upon decreasing the amount of V_6O_{13} nanobelts. The amount of the catalysts and the peak temperature and reversible capacity of dehydrogenation from MgH_2 catalyzed by V_6O_{13} nanobelts are among the best reported using various catalysts so far (Fig. 6f).

3. Conclusion

In this work, two-dimensional V_6O_{13} nanobelts with a thickness of 11 nm, which promote the uniform formation of metallic V inside of MgH_2, are fabricated to improve hydrogen storage performance of MgH_2. It is theoretically and experimentally demonstrated that metallic V not only enhances the H_2 desorption properties of MgH_2, but also facilitates its reversible H_2 adsorption process. Under the catalysis of metallic V, the energy for H_2 desorption of MgH_2 is reduced to 49.5 kJ mol^{-1}, 10.9 kJ mol^{-1} lower than that of the pristine counterpart, and the energy required for H_2 adsorption and dissociation is also decreased to −5.904 and 0.023 eV, respectively, which are much lower than those of the bulk counterpart, indicting its superior catalytic effect for improving the hydrogen storage performance of MgH_2. The introduction of V leads to strong bonding interactions between V and H, weaker structural stability, and higher surface states, which account for the dramatic decline of the H_2 desorption and adsorption energy barrier. As a result, the peak temperature for H_2 desorption of MgH_2 under the catalysis of 3 wt% V_6O_{13} nanobelts decreases to 221 °C, 101 °C lower than that of pristine MgH_2 and only 10 min is required for complete dehydrogenation of MgH_2 under the catalysis of V_6O_{13} nanobelts at 250 °C. More interestingly, even at room temperature, about 5.4 wt% H_2 could be recharged into the dehydrogenated MgH_2 within 12 h under the catalysis of V_6O_{13} nanobelts, and a systematic H_2 storage capacity of 6.8 wt% could be achieved within 10 cycles of hydrogenation and dehydrogenation process at 250 °C. This study provides a promising strategy to develop advanced V-based catalysts for improving the hydrogen storage performance of MgH_2.

Conflicts of interest

The authors declare no conflict of interest.

Acknowledgements

Y. M. and J. Z. contributed equally to this work. This work was financially supported by the National Key R&D Program of China (no. 2021YFB3802400), the National Natural Science Foundation of China (22279020, 51971065, 51901045, U2130208, and 52071156), the Science and Technology Commission of Shanghai Municipality (no. 21ZR1407500), and the Innovation Program of Shanghai Municipal Education Commission (2019-01-07-00-07-E00028).

References

1 L. Schlapbach and A. Zuttel, *Nature*, 2001, **414**, 353–358.
2 A. Zaluska, L. Zaluski and J. O. Strom-Olsen, *J. Alloys Compd.*, 1999, **288**, 217–225.
3 K. J. Jeon, H. R. Moon, A. M. Ruminski, B. Jiang, C. Kisielowski, R. Bardhan and J. J. Urban, *Nat. Mater.*, 2011, **10**, 286–290.
4 J. K. Ye, G. L. Xia and X. B. Yu, *Mater. Today Energy*, 2021, **22**, 100885.
5 W. Chen, Y. Sun, T. Xu, J. Ye, G. Xia, D. Sun and X. Yu, *ACS Appl. Energy Mater.*, 2022, **5**, 10501–10508.
6 Y. H. Sun, C. Q. Shen, Q. W. Lai, W. Liu, D. W. Wang and K. F. Aguey-Zinsou, *Energy Storage Mater.*, 2018, **10**, 168–198.
7 Q. Luo, J. D. Li, B. Li, B. Liu, H. Y. Shao and Q. Li, *J. Magnesium Alloys*, 2019, **7**, 58–71.
8 X. Yu, Z. Tang, D. Sun, L. Ouyang and M. Zhu, *Prog. Mater. Sci.*, 2017, **88**, 1–48.
9 X. L. Zhang, Y. F. Liu, X. Zhang, J. J. Hu, M. X. Gao and H. G. Pan, *Mater. Today Nano*, 2020, **9**, 100064.
10 X. Y. Zhang, Y. H. Sun, S. L. Ju, J. K. Ye, X. C. Hu, W. Chen, L. Yao, G. L. Xia, F. Fang, D. L. Sun and X. B. Yu, *Adv. Mater.*, 2023, **35**, 2206946.
11 M. S. Yahya and M. Ismail, *J. Phys. Chem. C*, 2018, **122**, 11222–11233.
12 X. Zhang, Z. Leng, M. Gao, J. Hu, F. Du, J. Yao, H. Pan and Y. Liu, *J. Power Sources*, 2018, **398**, 183–192.
13 Z. Ma, J. Zou, D. Khan, W. Zhu, C. Hu, X. Zeng and W. Ding, *J. Mater. Sci. Technol.*, 2019, **35**, 2132–2143.
14 L. Zhang, Z. Cai, Z. Yao, L. Ji, Z. Sun, N. Yan, B. Zhang, B. Xiao, J. Du, X. Zhu and L. Chen, *J. Mater. Chem. A*, 2019, **7**, 5626–5634.
15 M. Zhang, X. Z. Xiao, X. W. Wang, M. Chen, Y. H. Lu, M. J. Liu and L. X. Chen, *Nanoscale*, 2019, **11**, 7465–7473.
16 H. Gao, Y. Shao, R. Shi, Y. Liu, J. Zhu, J. Liu, Y. Zhu, J. Zhang, L. Li and X. Hu, *ACS Appl. Mater. Interfaces*, 2020, **12**, 47684–47694.
17 S. Milosevic, S. Kurko, L. Pasquini, L. Matovic, R. Vujasin, N. Novakovic and J. G. Novakovic, *J. Power Sources*, 2016, **307**, 481–488.

18 K. C. Xian, M. H. Wu, M. X. Gao, S. Wang, Z. L. Li, P. Y. Gao, Z. H. Yao, Y. F. Liu, W. P. Sun and H. G. Pan, *Small*, 2022, **18**, 2107013.
19 Z. Y. Wang, X. L. Zhang, Z. H. Ren, Y. Liu, J. J. Hu, H. W. Li, M. X. Gao, H. G. Pan and Y. F. Liu, *J. Mater. Chem. A*, 2019, **7**, 14244–14252.
20 M. El Khatabi, M. Bhihi, S. Naji, H. Labrim, A. Benyoussef, A. El Kenz and M. Loulidi, *Int. J. Hydrogen Energy*, 2016, **41**, 4712–4718.
21 Y. T. Shao, H. G. Gao, Q. K. Tang, Y. N. Liu, J. C. Liu, Y. F. Zhu, J. G. Zhang, L. Q. Li, X. H. Hu and Z. X. Ba, *Appl. Surf. Sci.*, 2022, **585**, 152561.
22 L. Ren, W. Zhu, Y. H. Li, X. Lin, H. Xu, F. Z. Sun, C. Lu and J. X. Zou, *Nano-Micro Lett.*, 2022, **14**, 144.
23 H. Y. Wan, X. Yang, S. M. Zhou, L. Ran, Y. F. Lu, Y. A. Chen, J. F. Wang and F. S. Pan, *J. Mater. Sci. Technol.*, 2023, **149**, 88–98.
24 J. X. Zhang, H. Liu, C. S. Zhou, P. Sun, X. Y. Guo and Z. Z. Fang, *J. Mater. Chem. A*, 2023, **11**, 4789–4800.
25 Y. Zhao, T. Li, H. X. Huang, T. T. Xu, B. G. Liu, B. Zhang, J. G. Yuan and Y. Wu, *J. Mater. Sci. Technol.*, 2023, **137**, 176–183.
26 B. P. Mamula, J. G. Novakovic, I. Radisavljevic, N. Ivanovic and N. Novakovic, *Int. J. Hydrogen Energy*, 2014, **39**, 5874–5887.
27 L. T. Zhang, Z. L. Cai, X. Q. Zhu, Z. D. Yao, Z. Sun, L. Ji, N. H. Yan, B. B. Xiao and L. X. Chen, *J. Alloys Compd.*, 2019, **805**, 295–302.
28 B. Liu, B. Zhang, X. Chen, Y. Lv, H. Huang, J. Yuan, W. Lv and Y. Wu, *Mater. Today Nano*, 2022, **17**, 100168.
29 M. Chen, Y. Q. Wang, X. Z. Xiao, Y. H. Lu, M. Zhang, J. G. Zheng and L. X. Chen, *Appl. Surf. Sci.*, 2021, **541**, 148375.
30 Y. K. Fu, L. Zhang, Y. Li, S. Y. Guo, Z. C. Yu, W. F. Wang, K. L. Ren, Q. M. Peng and S. M. Han, *J. Mater. Sci. Technol.*, 2023, **138**, 59–69.
31 C. L. Lu, H. Z. Liu, L. Xu, H. Luo, S. X. He, X. Q. Duan, X. T. Huang, X. H. Wang, Z. Q. Lan and J. Guo, *J. Magnesium Alloys*, 2022, **10**, 1051–1065.
32 Z. Y. Wang, Z. H. Ren, N. Jian, M. X. Gao, J. J. Hu, F. Du, H. G. Pan and Y. F. Liu, *J. Mater. Chem. A*, 2018, **6**, 16177–16185.
33 X. L. Zhang, X. Zhang, L. C. Zhang, Z. G. Huang, F. Fang, Y. X. Yang, M. X. Gao, H. G. Pan and Y. F. Liu, *J. Mater. Sci. Technol.*, 2023, **144**, 168–177.
34 J. H. Zang, S. F. Wang, F. Wang, Z. Y. Long, F. J. Mo, Y. H. Xia, F. Fang, Y. Song and D. L. Sun, *J. Mater. Chem. A*, 2020, **8**, 14935–14943.
35 H. Liu, C. Lu, X. Wang, L. Xu, X. Huang, X. Wang, H. Ning, Z. Lan and J. Guo, *ACS Appl. Mater. Interfaces*, 2021, **13**, 13235–13247.
36 Z. Q. Lan, X. B. Wen, L. Zeng, Z. Q. Luo, H. R. Liang, W. T. Shi, F. F. Hong, H. Z. Liu, H. Ning, W. Z. Zhou and J. Guo, *Chem. Eng. J.*, 2022, **446**, 137261.
37 H. Gao, R. Shi, J. Zhu, Y. Liu, Y. Shao, Y. Zhu, J. Zhang, L. Li and X. Hu, *Appl. Surf. Sci.*, 2021, **564**, 150302.
38 Z. Q. Lan, H. Fu, R. L. Zhao, H. Z. Liu, W. Z. Zhou, H. Ning and J. Guo, *Chem. Eng. J.*, 2022, **431**, 133985.
39 K. Wang, X. Zhang, Y. Liu, Z. Ren, X. Zhang, J. Hu, M. Gao and H. Pan, *Chem. Eng. J.*, 2021, **406**, 126831.
40 M. Zhang, X. Z. Xiao, B. S. Luo, M. J. Liu, M. Chen and L. X. Chen, *J. Energy Chem.*, 2020, **46**, 191–198.
41 L. Zhang, K. Wang, Y. Liu, X. Zhang, J. Hu, M. Gao and H. Pan, *Nano Res.*, 2020, **14**, 148–156.
42 T. Czujko, R. A. Varin, C. Chiu and Z. Wronski, *J. Alloys Compd.*, 2006, **414**, 240–247.
43 G. Liang, J. Huot, S. Boily, A. Van Neste and R. Schulz, *J. Alloys Compd.*, 1999, **292**, 247–252.
44 S. L. Ju, J. K. Ye, Y. Meng, G. L. Xia and X. B. Yu, *Adv. Energy Mater.*, 2022, **12**, 2201653.
45 P. G. He, J. H. Liu, X. D. Zhao, Z. P. Ding, P. Gao and L. Z. Fan, *J. Mater. Chem. A*, 2020, **8**, 10370–10376.
46 H. E. Kissinger, *Anal. Chem.*, 1957, **29**, 1702–1706.
47 C. S. Zhou, Z. G. Z. Fang, J. Lu and X. Y. Zhang, *J. Am. Chem. Soc.*, 2013, **135**, 10982–10985.